

# Iso-Propagation Vortices with OAM-independent Size and Divergence Towards Future Faster Optical Communications

Wenxiang Yan,<sup>1,2</sup> Zhaozhong Chen,<sup>4</sup> Xian Long,<sup>1,2</sup> Yuan Gao,<sup>1,2</sup> Zheng Yuan,<sup>1,2</sup> Zhi-Cheng Ren,<sup>1,2</sup> Xi-Lin Wang,<sup>1,2</sup> Jianping Ding,<sup>1,2,3,\*</sup> and Hui-Tian Wang<sup>1,2,\*</sup>

<sup>1</sup>National Laboratory of Solid State Microstructures and School of Physics, Nanjing University, Nanjing 210093, China

<sup>2</sup>Collaborative Innovation Center of Advanced Microstructures, Nanjing University, Nanjing 210093, China

<sup>3</sup>Collaborative Innovation Center of Solid-State Lighting and Energy-Saving Electronics, Nanjing University, Nanjing 210093, China

<sup>4</sup>James Watt School of Engineering, University of Glasgow, Glasgow, G12 8QQ, UK

\*Corresponding author: jpding@nju.edu.cn; htwang@nju.edu.cn

## Abstract

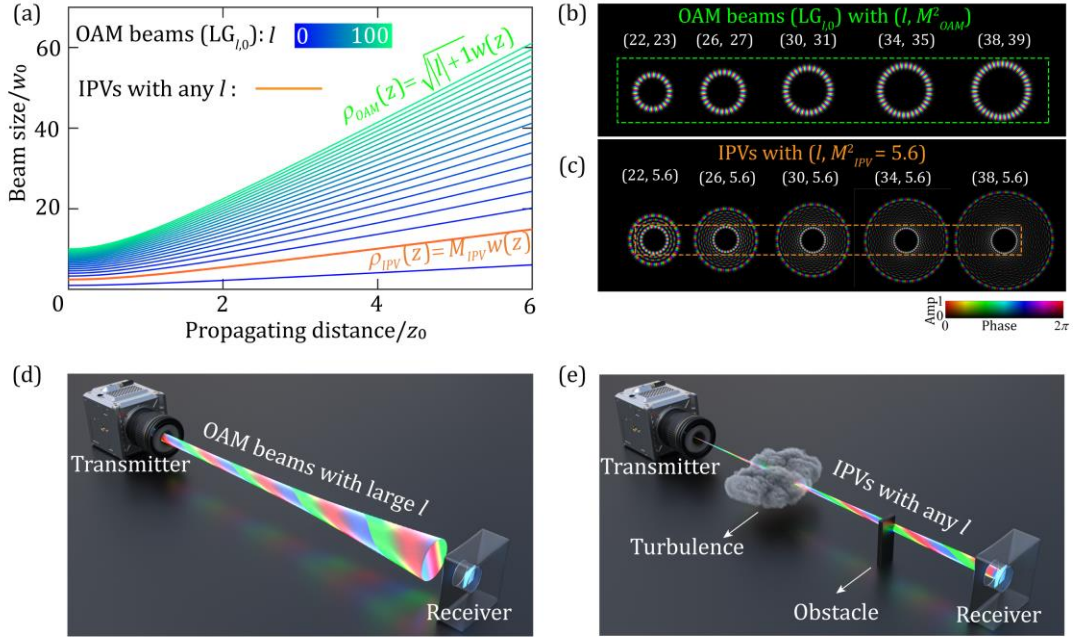
Recognized in the 1990s, vortex beams' ability to carry orbital angular momentum (OAM) has significantly contributed to applications in optical manipulation and high-dimensional classical and quantum information communication. However, inherent diffraction in free space results in the inevitable expansion of beam size and divergence contingent upon the OAM, limiting vortex beams' applicability in areas such as spatial mode multiplexing communication, fiber optic data transmission, and particle manipulation. These domains necessitate vortex beams with OAM-independent propagation characteristics. In this study, we introduce Iso-Propagation Vortices (IPVs), vortex beams characterized by OAM-independent propagation behavior; **achieved through precise radial index configuration of Laguerre-Gaussian beams**. IPVs display notable transmission dynamics, including a reduced quality factor, resilience post-damage, and decreased and uniform modal scattering under atmospheric turbulence. Their distinctive attributes render IPVs valuable for potential applications in imaging, microscopy, optical communication, metrology, quantum information processing, and light-matter interactions. Notably, within optical communication, the case study suggests that the IPV basis, due to its OAM-independent propagation behavior, provides access to a more extensive spectrum of data channels compared to conventional spatial multiplexing techniques, consequently augmenting information capacity.

## Introduction

Vortices are a widespread phenomenon in nature, appearing in diverse forms such as quantum vortices in liquid nitrogen, typhoon vortices, and spiral galaxies in the Milky Way, observable both in macroscopic matter and structured electromagnetic fields. As delineated by Allen et al.<sup>1</sup> in 1992, vortex fields have become a focal point of research in light fields due to their capability to carry orbital angular momentum (OAM). This property has garnered substantial interest across various sectors, encompassing high-dimensional classical and quantum information communications<sup>2-4</sup>, micro-particle manipulation<sup>5,6</sup>, optical measurements<sup>7,8</sup>, optical imaging<sup>9,10</sup>, and processing<sup>11-13</sup>. A persistent challenge encountered is light diffraction, which results in increased beam size and divergence as the mode index augments. This also makes it difficult to control the size of vortex beams with respect to the variation of the OAM index. We elucidate this phenomenon in Figs. 1(a) and (b) using prominent OAM beams, specifically a subset of Laguerre-Gaussian (LG) beams with a null radial index, (i.e.,  $p = 0$  for an  $LG_{l,p}$ , where  $l$  and  $p$  denoting the azimuthal and radial indices, respectively). This intrinsic diffraction-caused, OAM-dependent

1 propagation behavior limits the expansive applications of vortex fields. In the context of optical communication,  
 2 the behavior that the beam size and divergence of vortex beams increasing with OAM, necessitates larger receivers  
 3 for more modes and greater capacity, posing a constraint of the feasible capacity for spatial multiplexing especially  
 4 with realistically limited-size receivers<sup>14-17</sup>, as depicted in Fig. 1(d). While there have been endeavors to overcome  
 5 this limitation, conventional “perfect” vortex fields maintain OAM-independent size predominantly near a focal  
 6 plane and undergo degradation due to OAM-dependent divergence<sup>18, 19</sup>, as displayed in Figs. 2(a-f). To our  
 7 knowledge, vortex beams exhibiting OAM-independent size and divergence have not been reported.

8 In our research, we discerned that the innermost rings of LG beams display distinct dynamic transmission  
 9 properties: they possess a markedly small size and divergence, both of which can remain OAM-independent during  
 10 propagation with precise radial index configuration. These innermost rings, demonstrating OAM-independent  
 11 propagation, are hereby termed Iso-Propagation Vortices (IPVs). Due to their reduced and OAM-independent size  
 12 and divergence, IPVs undergo decreased and more consistent modal scattering in atmospheric turbulence. IPVs  
 13 also retain their structure post-damage. Their unique attributes render IPVs instrumental for potential applications  
 14 in imaging, microscopy, optical communication, metrology, quantum information processing, and light-matter  
 15 interactions. For instance, within the domain of optical communication, the case study indicates that the IPV basis,  
 16 endowed with OAM-independent propagation, enables access to a more expansive array of data channels  
 17 compared to traditional spatial multiplexing techniques, thus augmenting information capacity, as delineated in  
 18 Fig. 1(e).



19  
 20 **Fig. 1. Exploration of Conventional OAM beams versus IPVs.** (a) Traditional OAM beams (LG<sub>l,0</sub>)  
 21 showcase OAM-dependent size and divergence, with each color representing a unique OAM order *l*.  
 22 Conversely, IPVs manifest OAM-independent size and divergence (the orange curve), where  $M_{IPV}$  is  
 23 directly derived from the square root of the selected  $M^2_{IPV}$ . (b-c) Complex field patterns for OAM beams  
 24 (LG<sub>l,0</sub>) and IPVs with identical beam waist but varying OAM orders.  $M^2_{IPV}$  and  $M^2_{OAM}$ , are the quality  
 25 factors of IPVs and OAM beams (LG<sub>l,0</sub>). (d) Receivers with limited size obstruct the passage of OAM  
 26 beams having large *l* values due to increasing beam size and divergence as the mode index grows.  
 27 However, (e) IPVs of any *l* can easily traverse because of their OAM-independent propagation  
 28 characteristics, maintaining their structure even after turbulence or obstacles.

1

2 **Result**3 **Iso-Propagation Vortices with OAM-independent Size and Divergence**

4 The complex amplitude distribution of a normalized LG beam carrying OAM of  $l\hbar$  per photon in the cylindrical  
5 coordinate system  $(r, \varphi, z)$  is represented by<sup>20</sup>

$$6 \text{LG}_{l,p}(r, \varphi, z) = \sqrt{\frac{2p!}{\pi(|l|+p)!}} \frac{1}{w(z)} \left[ \frac{\sqrt{2}r}{w(z)} \right]^{|l|} L_p^{|l|} \left[ \frac{2r^2}{w^2(z)} \right] \exp\left(-\frac{r^2}{w^2(z)}\right) \quad (1)$$

$$\times \exp\left[ ikz + ik\frac{r^2}{2R(z)} + il\varphi - i(|l|+2p+1)\zeta(z) \right],$$

7 where  $L_p^l$  denotes the Laguerre polynomial with the azimuthal index  $l$  (or topological charge) and the radial index  
8  $p$ ,  $k=2\pi/\lambda$  is the wavenumber with  $\lambda$  being the wavelength, and

$$9 w(z) = w_0 \sqrt{1 + \left(\frac{z}{z_0}\right)^2}, \quad R(z) = z \left[ 1 + \left(\frac{z_0}{z}\right)^2 \right], \quad \zeta(z) = \tan^{-1}\left(\frac{z}{z_0}\right), \quad z_0 = \frac{\pi w_0^2}{\lambda}, \quad w_0 = \sqrt{\frac{\lambda z_0}{\pi}}, \quad (2)$$

10 with  $w_0$  denoting the beam waist at  $z = 0$ . The root-mean-squared waist radius (defines the size of the LG beam)

11  $\rho_{LG}(z) = \sqrt{|l|+2p+1}w(z)$  and divergence angle  $\theta_{LG} = \lim_{z \rightarrow \infty} d\rho_{LG}(z)/dz = \sqrt{|l|+2p+1}\theta_0$  describe the free-space

12 propagation property of the LG beam and are vital for the FSO communication<sup>21</sup>, where  $\theta_0$  is the divergence angle  
13 of the fundamental Gaussian beam. The beam quality factor<sup>22</sup> ( $M^2$ ), defined as the ratio between the space-  
14 bandwidth products of the LG beam,  $\rho_{LG}(0)\theta_{LG}$ , and of the fundamental Gaussian beam,  $w_0\theta_0$ , characterizes the  
15 propagation dynamics based on the inherent uncertainty principle between the beam size and divergence<sup>23</sup>

$$16 M_{LG}^2(l, p) = \frac{\rho_{LG}(0)\theta_{LG}}{w_0\theta_0} = |l|+2p+1. \quad (3)$$

17 From the relation  $\rho_{LG}(z) = M_{LG}(l, p)w(z)$  and  $\theta_{LG} = M_{LG}(l, p)\theta_0$ , we find an important characteristic: different LG beams  
18 with the same  $M_{LG}^2$  always hold the same size and the same divergence upon propagating, that is, they retain the  
19 same propagation dynamics. In addition, in most OAM-interplaying systems, OAM beams or vortex beams are

20 rendered by  $\text{LG}_{l,0}(r, \varphi, z)$ , i.e., a subset of LG beams with  $p = 0$ , whose beam size  $\rho_{OAM}(z) = \sqrt{|l|+1}w(z)$  (illustrated  
21 in Fig. 1(a)) and quality factor  $M_{OAM}^2(l) = |l|+1$  are both the smallest for each beam with OAM of  $l\hbar$  per photon.

22 After analyzing Eq. (1), we have derived the following analytical expression for the innermost ring size of the  
23 LG beam (i.e., the radius of the brightest ring, instead of the root-mean-squared waist radius, see Supplementary  
24 Text 1 for details)

$$25 \rho_{IR}(z) \approx \frac{|l|+2}{2\sqrt{|l|+2p+1}} w(z). \quad (4)$$

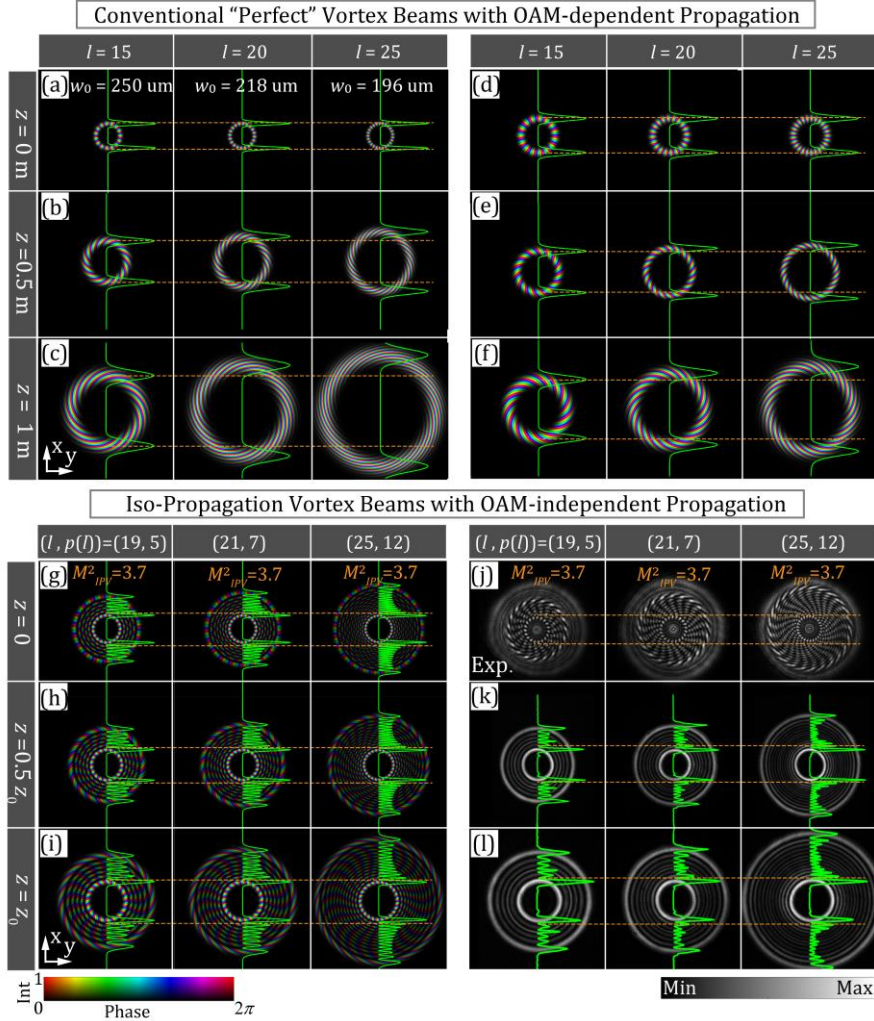
26 The subscript "IR" denotes the parameters related to the innermost ring for brevity. The divergence angle is given  
27 by

$$28 \theta_{IR} \approx \lim_{z \rightarrow \infty} d\rho_{IR}(z)/dz = \frac{|l|+2}{2\sqrt{|l|+2p+1}} \theta_0. \quad (5)$$

1 Consequently, the “quality factor” defined by the innermost ring can be written as

$$2 \quad M_{IR}^2(l, p) \approx \frac{\rho_{IR}(0)\theta_{IR}}{w_0\theta_0} = \frac{(|l|+2)^2}{4(|l|+2p+1)}. \quad (6)$$

3 Given a global quality factor as  $M_{IR}^2(l) = M_{IPV}^2$ , the radial index of beams can be determined by  $p(l) =$   
 4  $\text{round}((0.5|l|+1)^2/2M_{IPV}^2-0.5(|l|+1))$ , with the  $\text{round}(\cdot)$  function indicating rounding to the nearest integer. As per  
 5 Eqs. (4-6), this set of innermost rings, characterized by the global parameter  $M_{IPV}^2$ , exhibits an OAM-independent  
 6 size, given by  $\rho_{IPV}(z) = M_{IPV}w(z)$ , and also an OAM-independent divergence, denoted by  $\theta_{IPV} = M_{IPV}\theta_0$ . Consequently,  
 7 these rings demonstrate OAM-independent propagation behavior, as depicted in Figs. 2(g-l), and are denoted as  
 8 Iso-Propagation Vortices (IPVs). In contrast, conventional “perfect” vortices, which show OAM-independent radii  
 9 only near a specific plane (usually the focal plane), fail to maintain OAM-independent propagation because of OAM-  
 10 dependent divergence. Specifically, Perfect Laguerre–Gauss beams<sup>18</sup> compensate for the OAM-related expansion of  
 11 beam size at a certain plane (e.g.,  $z = 0$  m) by adjusting the beam waist ( $w_0$ ). **However, these results in OAM-**  
 12 **dependent divergence due to the variation in beam waist**, as depicted in Figs. 2(a-c). Similarly, a common form of  
 13 perfect vortex beam<sup>19</sup>, generated by Fourier transforming Bessel–Gauss beams, exhibits OAM-independent radii  
 14 solely in the focal plane ( $z = 0$  m). **Yet, it too cannot sustain OAM-independent propagation owing to OAM-**  
 15 **dependent divergence**, as shown in Figs. 2(d-f).



16  
 17 **Fig. 2. Demonstration of OAM-dependent and OAM-independent propagation.** The complex amplitude  
 18 distributions of (a-c) “Perfect Laguerre–Gauss beams” (ref. <sup>18</sup>) and (d-f) “Perfect vortex beam” (ref. <sup>19</sup>) at  $z = 0, 0.5$

m, 1 m, respectively.  $w_0$ , the beam waist at  $z = 0$ . (g-i) The complex amplitude distributions of the innermost-ring-based IPVs with global  $M^2_{IPV} = 3.7$  at  $z=0, 0.5z_0, z_0$ , respectively. (j-l) The corresponding experimental results for (g-i); especially, (j) is the interference patterns between the IPVs and a reference plane wave. The luminance and color of the colormap refer to the intensity (Int) and phase, respectively; the green curves represent intensity profiles along the  $x$ -axis and the horizontal orange-dashed lines serve as a reference for indicating the size of the vortex rings. For further experimental details, refer to Supplementary text 5.

### Transmission Characteristics of Iso-Propagation Vortices

**Superior transmission dynamics:** Eqs. (4-6) indicate that the IPV mode parameters ( $M^2, \rho, \theta$ ) exhibit an increase with the absolute value of topological charge ( $|l|$ ) while showing a decrease with the radial index ( $p$ ). This behavior contrasts with LG beams, where these parameters augment with both  $|l|$  and  $p$ . As a result, for a given topological charge  $l$ , IPVs display significantly lower values of parameters ( $M^2, \rho, \theta$ ) compared to conventional LG beams. In Figs. 3(a-d), we contrast  $M^2$  values for LG beams ( $M^2_{LG}(l, p)$ ) with those for IPV ( $M^2_{IPV}(l, p)$ ) across the initial 10,000 orders. This comparison highlights a wider dispersion range for  $M^2_{LG}(l, p)$ , spanning from 0 to 300, in contrast to  $M^2_{IPV}(l, p)$ , which primarily ranges between 0 and 20. Consequently, IPVs demonstrate superior transmission properties including reduced size, divergence, and enhanced quality factor, surpassing those of LG beams.

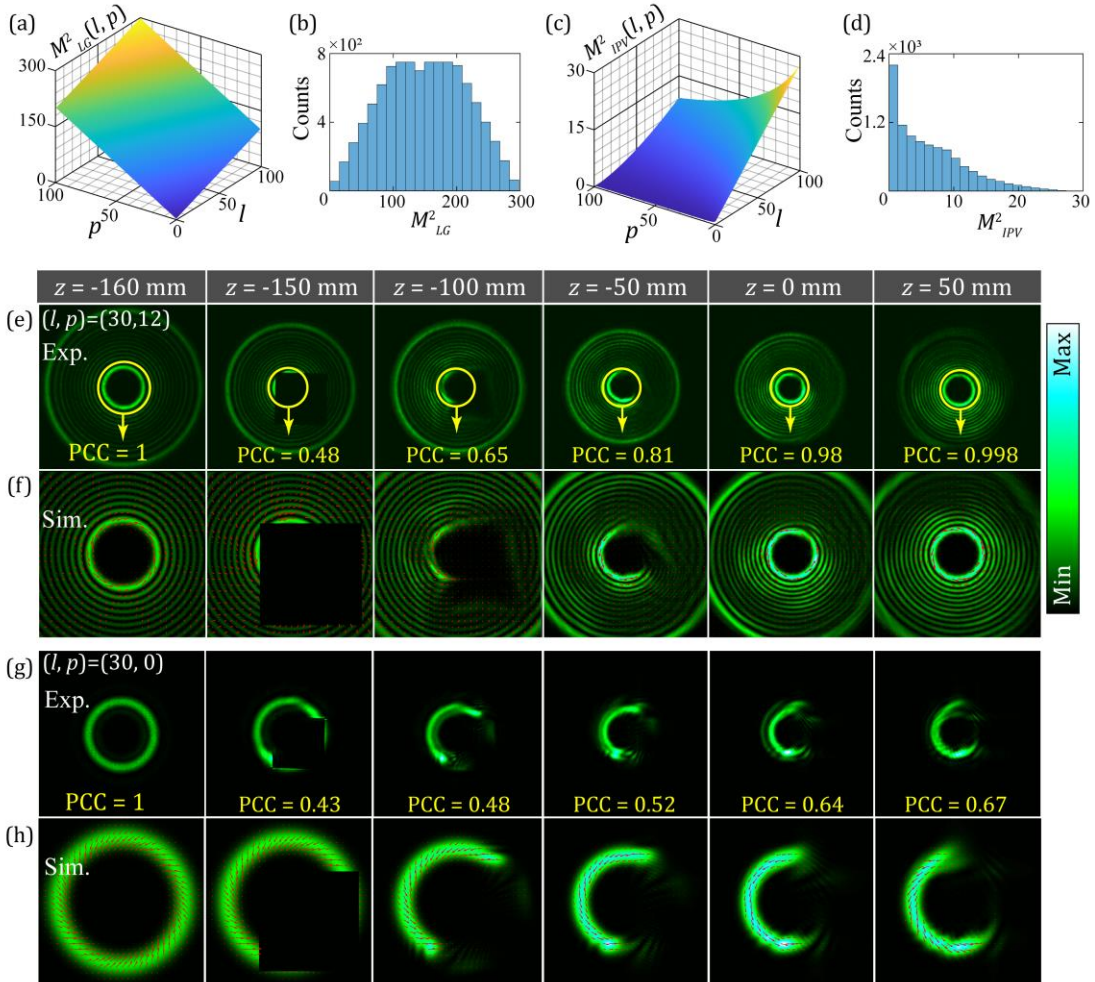
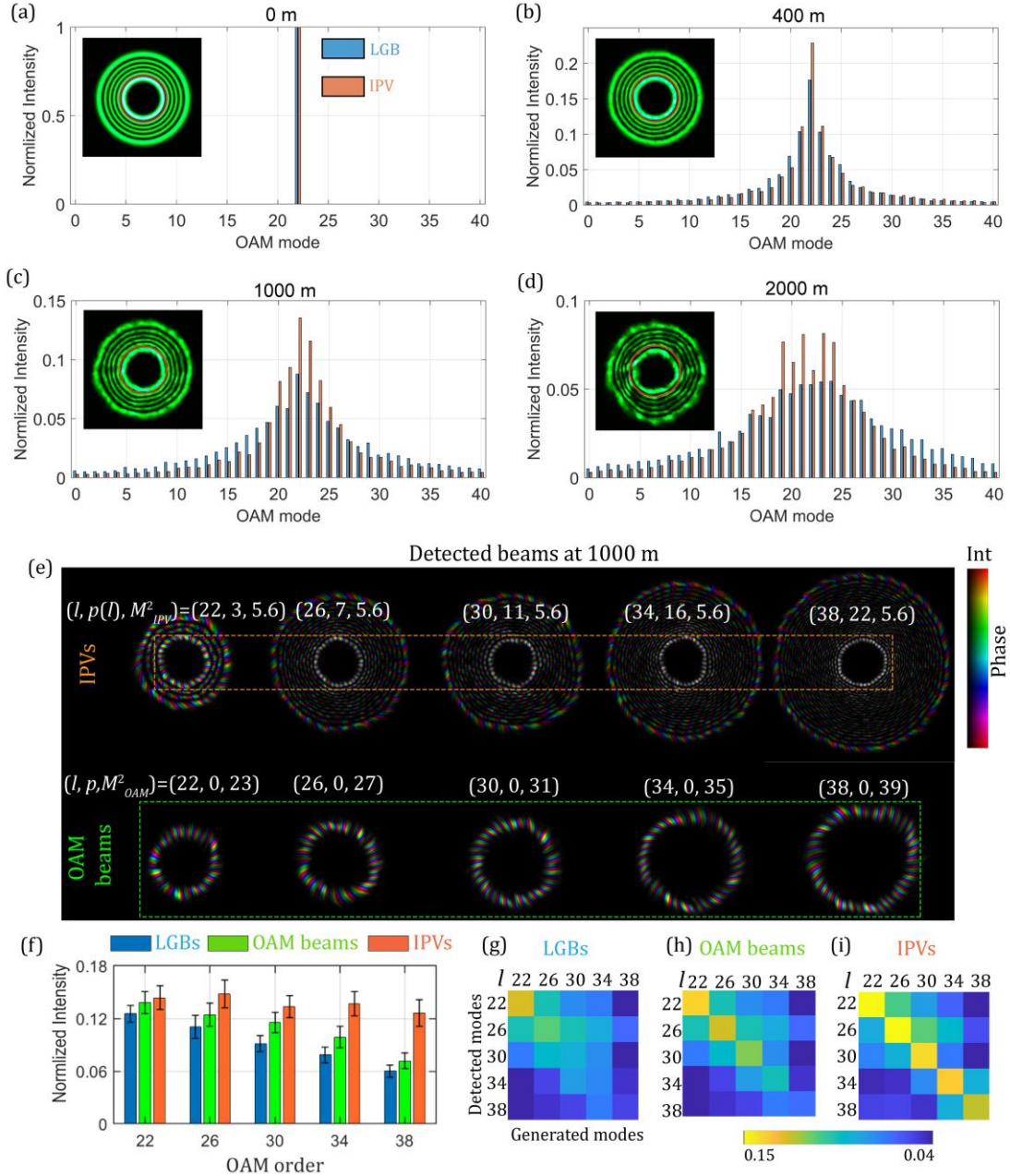


**Fig. 3. Smaller quality factors and self-healing properties of IPVs.** Quality factors of (a) LG beams- $M^2_{LG}(l, p)$  and (c) IPVs- $M^2_{IPV}(l, p)$  for 10000 lowest orders ( $l$  and  $p$  equal 0, 1, ..., 99 respectively; results for  $l < 0$  are the same as

1 those for  $l > 0$  and are omitted here). The corresponding distribution histograms are shown in (b) and (d). The IPV  
2 ( $l = 30, p = 12, z_0 = 150$  mm) is blocked by a square obstacle at  $z = -150$  mm: (e) Experimental intensity maps at  
3 different z-axial locations (Supplementary Movie S1, MP4, 732KB); (f) Transversal energy flow of (e), following  
4 from the cycle-average Poynting vector<sup>24</sup>, the red arrows indicate the value and direction of each flow  
5 (Supplementary Movie S2, MP4, 1.52MB), where **PCC is Pearson correlation coefficient of innermost rings**;  
6 (g-h) are the same as (e-f) but for OAM beams (i.e.,  $LG_{l0}$ ) (Supplementary Movies S3-S4, MP4, 358KB and 1.14MB).  
7 The sharp-edged square obstacle is produced as masks via the process of photoetching chrome patterns on a glass  
8 substrate. **For further experimental details, refer to Supplementary text 5.**  
9

10 **Self-restoration post-damage facilitated by sidelobes:** Another noteworthy property of IPVs is their self-  
11 rehabilitation. Post severe damage, these vortices tend to regenerate their original form, bolstered by sidelobes. In  
12 Fig. 3(e), we present experimental evidence of an IPV encountering an obstruction (a square-shaped obstacle). The  
13 IPV gradually restores its original structure over a certain distance, thanks to the support from its sidelobes. This  
14 experimental result was obtained using the setup detailed in the reference<sup>25</sup>, as well as in **Supplementary text 5.**  
15 Additionally, numerical simulations of the energy circulation within these vortices clarify how they recover: Figure  
16 3(f) unveils that while the IPV's energy flow is strong in the azimuthal (circular) direction, **the key to its**  
17 **regeneration lies predominantly in the radial (inward) component. This component draws energy from the outer**  
18 **sidelobes. Absent this "energy reserve" in sidelobes, the OAM beam's vortex ring fails to exhibit similar self-repair**  
19 **capabilities post-damage, as illustrated in Figs. 3(g-h). Such sidelobe-facilitated rejuvenation enhances the**  
20 **robustness of IPVs against disturbances, in contrast to OAM beams. To quantitatively describe the**  
21 **reconstruction of impaired IPVs in Figs. 3(e-f), we introduced the Pearson correlation coefficients (PCCs)**  
22 **between the intensity maps of IPVs at each z-axial location with and without the square obstacle. The**  
23 **Pearson correlation coefficients (PCCs) of matrices X and Y is defined by  $PCC(X, Y) = \text{cov}(X, Y) / \sigma_X \sigma_Y$ ,**  
24 **where  $\text{cov}(X, Y)$  is the covariance of X and Y and  $\sigma_X$  or  $\sigma_Y$  is the standard deviation of matrices X or Y.**  
25

26 **Reduced Modal Scattering in Atmospheric Turbulence:** Atmospheric turbulence, along with the  
27 diffraction-induced beam expansion, impedes the attainment of faster and more distant optical links<sup>26</sup>. **The relevant**  
28 **studies show that modal scattering exacerbates with escalating turbulence strength and beam size<sup>27</sup>.** As depicted  
29 in Figs. 4(a-d), in comparison to the LG beam, the IPV undergoes a relatively attenuated modal scattering effect due  
30 to atmospheric turbulence. Figs. 4(g-j) emphasize that, in contrast to traditional LG beams with OAM-dependent  
31 propagation dynamics, IPVs, **which have OAM-independent characteristics and reduced beam size and lower**  
32 **divergence (e.g.,  $M^2_{IPV} = 5.6$ ), encounter lesser and more uniform modal scattering across various mode orders.**  
33 Therefore, IPVs stand out as promising candidates for future developments in atmospheric communication  
34 multiplexing<sup>28-29</sup>. More detailed analysis and discussion can be found in Supplementary Text 2.



1  
2 **Fig. 4. Assessing Free-space Propagation Amidst Atmospheric Turbulence** for the LG beam and  
3 corresponding innermost-ring-based IPV with  $l = 22$  and  $p = 5$  in (a-d) from 0 to 2000 m. The insets display the  
4 intensity patterns of the propagating LG beam at different distances, while the red circles represent the aperture to  
5 truncate the innermost ring. (e) The complex distributions for detected beams of IPV with global  $M^2_{IPV} = 5.6$  and  
6 the corresponding OAM beams at  $z = 1000$  m against atmospheric turbulence; (f) The normalized intensity in  
7 detected modes for each launched mode in (e) at  $z = 1000$  m; (g-i) the crosstalk matrices for LG beams, OAM beams,  
8 and IPV.  
9

## 10 A case study in optical communication with Enhanced Capacity

11 The pursuit of greater capacity for information capture and processing remains an essential objective among  
12 researchers in the field of optical communication<sup>30</sup>. Optical multiplexing, leveraging degrees of freedom like  
13 polarization and wavelength, has historically augmented the capacity of both radiofrequency and optical  
14 communication systems<sup>31-33</sup>. Spatial mode-division multiplexing introduces a novel approach by utilizing

1 orthogonal spatial modes as distinct communication channels<sup>34-39</sup>. To illustrate, consider an FSO link that integrates  
 2 spatial mode-division multiplexing with  $Q$  orthogonal modes, polarization-division multiplexing with two distinct  
 3 polarization states, and wavelength-division multiplexing with  $T$  wavelengths. When encoded with 100 Gbit/s  
 4 quadrature phase-shift keying data, this configuration can achieve a collective capacity of  $Q \times 2 \times T \times 100$  Gbit/s. This  
 5 capacity can escalate to several Pbit/s (ref. <sup>37</sup>), offering the promise of advancing both deep-space and proximate  
 6 Earth optical communications by substantially elevating capacity and spectral efficiency. However, the prevailing  
 7 implementation of spatial mode-division multiplexing encounters a formidable impediment<sup>14-17</sup>. Inherent  
 8 diffraction causes an inevitable increase in beam size and divergence concomitant with the rising mode indices,  
 9 including the OAM index in vortex beams. These results in a prerequisite for larger receivers to accommodate  
 10 higher capacities involving more modes. This need frequently clashes with the practical size constraints of such  
 11 receivers, critically curbing the capacity potential of contemporary spatial mode-division multiplexing, as  
 12 delineated in Fig. 1(d).

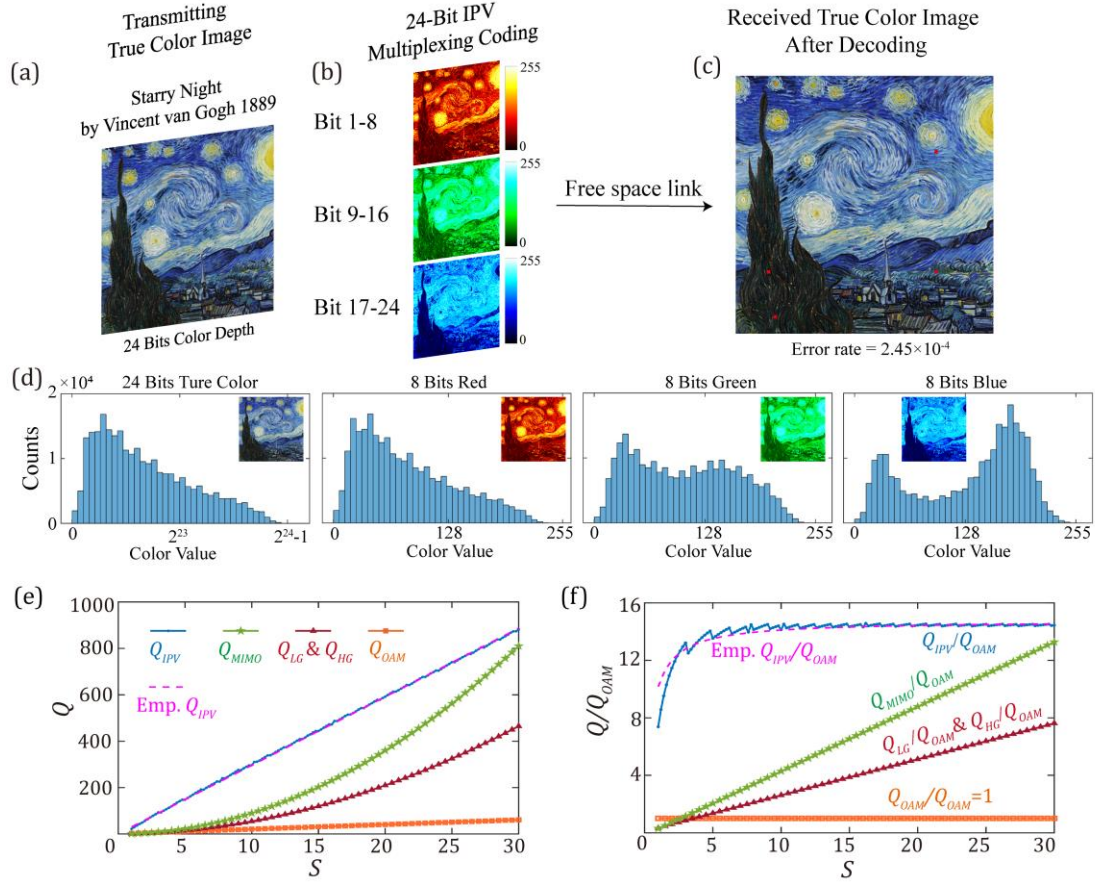
13 Employing the IPV basis, given its OAM-independent propagation characteristics, avails access to an  
 14 expanded suite of subchannels compared to conventional spatial multiplexing approaches, thus enhancing the  
 15 information capacity for feasible free-space optical systems, as delineated in Fig. 1(e). To validate this, the number  
 16 of IPV's suitable for a line-of-sight free-space communication system characterized by a space-bandwidth product  
 17 (SBP) of  $(2R_0 \times 2NA/\lambda)$  was determined, where  $R_0$  and NA are the aperture radius and numerical aperture of both  
 18 circular apertures of transmitter and receiver, and  $\lambda$  is the wavelength. Following the procedure of ref. <sup>40</sup>, the system  
 19 quality factor, denoted as  $S = \pi R_0 \times NA/\lambda$ , which is a dimensionless parameter and is  $\pi/4$  times the SBP, was  
 20 ascertained. Only beams with a quality factor less than the system's  $S$  value can traverse this system. The solution  
 21 count for  $M^2 \leq S$  provides the system's  $Q$  value. For example, when employing the LG beam multiplexing as the  
 22 information carrier, the addressable subchannels can be computed as  $Q_{LG}(S) \approx 0.5 \text{floor}[S](\text{floor}[S]+1)$  by resolving  
 23  $M^2_{LG}(l, p) = |l| + 2p + 1 \leq S$ . Analogously, the numbers of addressable subchannels for conventional OAM beam  
 24 multiplexing, Hermite-Gaussian beam multiplexing and multi-input multi-output transmission are as follows:  
 25  $Q_{OAM}(S) \approx 2 \text{floor}[S] + 1$ ,  $Q_{HG}(S) = Q_{LG} \approx 0.5 \text{floor}[S](\text{floor}[S]+1)$ , and  $Q_{MIMO}(S) = \text{round}[0.9S^2]$ , respectively<sup>40</sup>.

26 When  $M^2_{IPV}$  is set to be less than  $S$ , it ensures compatibility between IPV's with mode indices  $(l, p(l))$  and the  
 27 FSO system characterized by the system quality factor  $S$ , resulting in a more substantial subchannel array. It is  
 28 imperative to recognize that currently available spatial light modulators present constraints associated with panel  
 29 and pixel dimensions, impacting the precise projection of structured beams with elevated mode orders. However,  
 30 preliminary experiments (Supplementary Text 3) incorporating 105 IPV subchannels (Supplementary Movie S5,  
 31 MP4, 1.81MB) with  $l = [-52, 52]$ ,  $S = 6.25$ , and  $M^2_{IPV} = 0.9S = 5.6$ , manifest the pronounced enhancements of  $Q$  for IPV  
 32 multiplexing compared to traditional methodologies. These enhancements range from 300% to 808% in contrast  
 33 to  $Q_{OAM}(S=6.25) = 13$ ,  $Q_{LG}(S=6.25) = Q_{HG}(S=6.25) = 21$ ,  $Q_{MIMO}(S=6.25) = 35$ . The number of IPV subchannels can be  
 34 further boosted by the adoption of metasurface platforms with large panel sizes and ultra-high resolution. When  
 35 factoring in inter-channel crosstalk in mode-multiplexed communication, it is customary to select subchannels  
 36 within specific mode intervals. Nevertheless, a higher subchannel limit ( $Q$ ) for multiplexing corresponds to a  
 37 greater number of practically applicable subchannels and enhanced capacity.

38 Figure 5 presents an illustrative example of this concept, showcasing an IPV-multiplexed transmission of  
 39 Vincent van Gogh's iconic artwork "Starry Night." This artwork, rendered in true color, was segmented into RGB  
 40 layers. Each layer was encoded with 8-bit color depth, and the color distribution histograms are presented in Fig.  
 41 5(b). The conveyed information per pixel was channeled via 24-bit IPV multiplexing, ensuring exceptional color  
 42 fidelity. Bits 1-24 correspond to  $l = [52, -50, 48, -46, 44, -42, 40, -38, 32, -30, 28, -26, 24, -22, 20, -18, 16, -14, 12, -10,$   
 43  $8, -6, 4, -2]$  with  $M^2_{IPV} = 5.6$ . Upon receiving and decoding the high-density data streams of  $128 \times 128 \times 24$  bits from the  
 44 experimental setup of Supplementary Text 3, we successfully recovered the true color image with an ultra-high



1 color fidelity. The error rate was impressively low at  $2.45 \times 10^{-4}$ , much lower than the forward error correction limit  
 2 of  $3.8 \times 10^{-3}$ , as shown in Fig. 5(c). Figure 5(d) shows the color distribution histograms of this true-color image with  
 3 24 bits color depth and the RGB layers with 8 bits color depth. In this proof-of-principle experiment, the highest  
 4 transmission rate reached  $24 \times 11k = 0.264$  Mbit/s when using digital mirror devices at an 11 kHz refresh rate.  
 5



6  
 7 **Fig. 5. Image transmission by 24-bit IPV multiplexing with ultra-high color fidelity.** (a) True color image,  
 8 Starry Night by Vincent van Gogh 1889, with 24 bits color depth and  $2^{24}$  colors including  $128 \times 128$  pixels; (b) Three  
 9 RGB layers of (a) and were encoded from Bit 1 to 24; (c) Received true color image after recovering with an error  
 10 rate =  $2.45 \times 10^{-4}$ . (d) Color distribution histograms of the true color image with 24 bits color depth and the RGB  
 11 layers with 8 bits color depth. The red pixels indicate the incorrect data received. (e) Numbers  $Q$  of independent  
 12 spatial subchannels for spatial multiplexing techniques from  $S = 1$  to  $S = 30$ ; Emp.: Empirical. (f) The improvement  
 13 of numbers of independent spatial subchannels in (e) versus  $Q_{OAM}$ .  
 14

15 For a more comprehensive comparison of subchannels of different spatial multiplexing techniques, we  
 16 calculated  $Q_{IPV}$  with different  $S$  using the empirical formula  $Q_{IPV} \approx 2 \text{floor}[14.76S] + 1$  (Emp.  $Q_{IPV}$ , the pink-dashed  
 17 curve in Fig. 5(e)), which agrees well with the actual results ( $Q_{IPV}$ , the blue curve) in Fig. 5(e) (See details in  
 18 Supplementary Text 4). This approach attains an approximate 14-fold improvement for most systems compared  
 19 with traditional OAM multiplexing of  $Q_{OAM} \approx 2 \text{floor}[S] + 1$ . For practical FSO systems with limited-size receivers and  
 20  $S < 30$ , IPV multiplexing offers more subchannels than spatial multiplexing technique<sup>36</sup>, such as LG beam  
 21 multiplexing, HG beam multiplexing, and conventional MIMO transmission, as illustrated in Figs. 5(e) and (f). In  
 22 comparison with the latest work on structured light, specifically multi-vortex geometric (MVG) beam  
 23 multiplexing<sup>32</sup>, for the practical FSO systems with limited-size receivers and  $S < 30$ ,  $Q_{MVG}$  for MVG beam multiplexing

1 is close to  $Q_{LG}$ , and thus also lower than  $Q_{IPV}$ . For instance, in the aforementioned preliminary experiments with  
2 given  $S = 6.25$ , the estimated  $Q_{IPV} = 185$ , in contrast to  $Q_{OAM} = 13$ ,  $Q_{LG} (Q_{HG}) = 21$ ,  $Q_{MIMO} = 35$ , respectively.  
3

## 4 **Conclusion**

5 In conclusion, the amplification of beam size and divergence due to diffraction-induced influences and the  
6 increase in mode indices (e.g., OAM) pose significant constraints on the applicability of vortex beams in areas such  
7 as spatial mode multiplexing communication, fiber optic data transmission, and particle manipulation. The OAM-  
8 expansion propagation behavior, in particular, considerably restricts the feasible capacity for free-space optical  
9 links. In response to the need for vortex beams with OAM-independent propagation features, this study introduced  
10 Iso-Propagation Vortices (IPVs), characterized by their OAM-independent size and divergence during propagation.  
11 Beyond Iso-Propagation with respect to OAM, IPVs exhibit distinctive transmission dynamics, including enhanced  
12 resilience post-damage, diminished quality factor, and reduced, uniform modal scattering under atmospheric  
13 disturbances. These properties position IPVs as potentially valuable tools for diverse applications. **Comparison**  
14 **table among traditional vortex beams, perfect vortex beams, and Iso-Propagation vortex beams is shown in Table**  
15 **S2 in Supplementary Text 6. In optical communication, for example, the IPV basis could expand available data**  
16 **channels, potentially surpassing traditional spatial multiplexing methods and thus boosting information capacity.**  
17 **Additionally, the resilience of IPVs to damage and their consistent propagation characteristics may be beneficial in**  
18 **imaging and microscopy, possibly improving resolution and contrast. In quantum information processing, the**  
19 **ability of IPVs to maintain their structure post-damage and exhibit reduced modal scattering under atmospheric**  
20 **turbulence could be advantageous, although further research is needed to fully realize these applications. Similarly,**  
21 **the unique properties of IPVs might be exploited in studies of light-matter interactions, with potential applications**  
22 **in fields ranging from material science to optoelectronics. In summary, while the practical applications of IPVs hold**  
23 **promise, further research is necessary to fully understand their potential and to develop the technology for**  
24 **widespread use in various fields.**  
25

## 26 **Data availability**

27 All data that support the findings of this study are available within the article and Supplementary Information, or  
28 available from the corresponding author on reasonable request.  
29

## 30 **Acknowledgements**

31 This work was financially supported by National Key Research and Development Program of China  
32 (2023YFA1406903, 2022YFA1404800) and National Natural Science Foundation of China (12374307, 12234009,  
33 12274215).

## 34 **Author contributions**

35 W.Y. and J.D. proposed the original idea and designed the study. W. Y. built the experimental system and performed  
36 the experiments. C.Z., X.L., Y.G., and Z.Y. assisted the experiments. J.D. and H.T.W. supervised the project. All authors  
37 contributed to writing the manuscript.

## 38 **Competing interests**

39 The authors declare no competing interests

## Reference

1. L. Allen et al., "Orbital angular momentum of light and the transformation of laguerre-gaussian laser modes," *Phys. Rev. A* **45**(11), 8185-8189 (1992).
2. J. Wang et al., "Tailoring light on three-dimensional photonic chips: A platform for versatile oam mode optical interconnects," *Adv. Photon.* **5**(3), 036004-036004 (2023).
3. A. Suprano et al., "Orbital angular momentum based intra-and interparticle entangled states generated via a quantum dot source," *Adv. Photon.* **5**(4), 046008-046008 (2023).
4. Q. Cao et al., "Propagation of transverse photonic orbital angular momentum through few-mode fiber," *Adv. Photon.* **5**(3), 036002-036002 (2023).
5. E. Brasselet, "Torsion pendulum driven by the angular momentum of light: Beth's legacy continues," *Adv. Photon.* **5**(3), 034003-034003 (2023).
6. J. Zhang et al., "Generation of time-varying orbital angular momentum beams with space-time-coding digital metasurface," *Adv. Photon.* **5**(3), 036001-036001 (2023).
7. X. Li, Y. Tai and Z. Nie, "Digital speckle correlation method based on phase vortices," *Opt. Eng.* **51**(7), 077004 (2012).
8. Z. Lin et al., "Single-shot kramers-kronig complex orbital angular momentum spectrum retrieval," *Adv. Photon.* **5**(3), 036006-036006 (2023).
9. A. Chmyrov et al., "Nanoscopy with more than 100,000' doughnuts'," *Nat. methods* **10**(8), 737-740 (2013).
10. N. Zhang et al., "Multiparameter encrypted orbital angular momentum multiplexed holography based on multiramp helicoconical beams," *Adv. Photon. Nexus* **2**(3), 036013-036013 (2023).
11. S. Khonina et al., "The phase rotor filter," *J. Mod. Opt.* **39**(5), 1147-1154 (1992).
12. J. Yan and G. Geloni, "Self-seeded free-electron lasers with orbital angular momentum," *Adv. Photon. Nexus* **2**(3), 036001-036001 (2023).
13. Y. Zang, A. Mirando and A. Chong, "Spatiotemporal optical vortices with arbitrary orbital angular momentum orientation by astigmatic mode converters," *Nanophotonics* **11**(4), 745-752 (2022).
14. A. E. Willner et al., "Design challenges and guidelines for free-space optical communication links using orbital-angular-momentum multiplexing of multiple beams," *J. Opt.* **18**(7), 074014 (2016).
15. G. Xie et al., "Performance metrics and design considerations for a free-space optical orbital-angular-momentum-multiplexed communication link," *Optica* **2**(4), 357-365 (2015).
16. M. Krenn et al., "Communication with spatially modulated light through turbulent air across vienna," *New J. Phys.* **16**(11), 113028 (2014).
17. M. Krenn et al., "Twisted light transmission over 143 km," *Proc. Natl. Acad. Sci.* **113**(48), 13648-13653 (2016).
18. J. Mendoza-Hernández et al., "Perfect laguerre-gauss beams," *Opt. Lett.* **45**(18), 5197-5200 (2020).
19. P. Vaity and L. Rusch, "Perfect vortex beam: Fourier transformation of a bessel beam," *Opt. Lett.* **40**(4), 597-600 (2015).
20. Saleh B E A, Teich M C. *Fundamentals of photonics*[M]. john Wiley & sons, 2019.
21. R. L. Phillips and L. C. Andrews, "Spot size and divergence for laguerre gaussian beams of any order," *Appl. Opt.* **22**(5), 643-644 (1983).
22. A. E. Siegman, "New developments in laser resonators," *Optical resonators* 2-14 (1990).
23. M. Padgett, "On the focussing of light, as limited by the uncertainty principle," *J. Mod. Opt.* **55**(18), 3083-3089 (2008).
24. A. Bekshaev, K. Y. Bliokh and M. Soskin, "Internal flows and energy circulation in light beams," *J. Opt.*

- 1       13(5), 053001 (2011).
- 2   25. W. Yan et al., "Non-diffracting and self-accelerating bessel beams with on-demand tailored intensity  
3       profiles along arbitrary trajectories," *Opt. Lett.* **46**(7), 1494-1497 (2021).
- 4   26. A. Forbes, M. de Oliveira and M. R. Dennis, "Structured light," *Nat. Photonics* **15**(4), 253-262 (2021).
- 5   27. A. Klug, I. Nape and A. Forbes, "The orbital angular momentum of a turbulent atmosphere and its impact  
6       on propagating structured light fields," *New J. Phys.* **23**(9), 093012 (2021).
- 7   28. B. B. Yousif and E. E. Elsayed, "Performance enhancement of an orbital-angular-momentum-multiplexed  
8       free-space optical link under atmospheric turbulence effects using spatial-mode multiplexing and hybrid  
9       diversity based on adaptive mimo equalization," *IEEE Access* **7**, 84401-84412 (2019).
- 10  29. B. B. Yousif, E. E. Elsayed and M. M. Alzalabani, "Atmospheric turbulence mitigation using spatial mode  
11       multiplexing and modified pulse position modulation in hybrid rf/fso orbital-angular-momentum  
12       multiplexed based on mimo wireless communications system," *Opt. Commun.* **436**, 197-208 (2019).
- 13  30. C. E. Shannon, "A mathematical theory of communication," *ACM SIGMOBILE mobile computing and  
14       communications review* **5**(1), 3-55 (2001).
- 15  31. L. Hanzo et al., *Quadrature amplitude modulation: From basics to adaptive trellis-coded, turbo-equalised  
16       and space-time coded ofdm, cdma and mc-cdma systems*, IEEE Press-John Wiley (2004).
- 17  32. S. G. Evangelides et al., "Polarization multiplexing with solitons," *J. Lightwave Technol.* **10**(1), 28-35  
18       (1992).
- 19  33. B. Mukherjee, *Optical WDM networks*, Springer Science & Business Media (2006).
- 20  34. J. Wang et al., "Terabit free-space data transmission employing orbital angular momentum multiplexing,"  
21       *Nat. Photonics* **6**(7), 488-496 (2012).
- 22  35. N. Bozinovic et al., "Terabit-scale orbital angular momentum mode division multiplexing in fibers,"  
23       *Science* **340**(6140), 1545-1548 (2013).
- 24  36. Z. Wan et al., "Divergence-degenerate spatial multiplexing towards future ultrahigh capacity, low error-  
25       rate optical communications," *Light Sci. Appl.* **11**(1), 1-11 (2022).
- 26  37. J. Wang et al., "N-dimensional multiplexing link with 1.036-pbit/s transmission capacity and 112.6-  
27       bit/s/hz spectral efficiency using ofdm-8qam signals over 368 wdm pol-muxed 26 oam modes," *2014  
28       The European Conference on Optical Communication (ECOC)* 1-3 (2014).
- 29  38. J. Wang et al., "Orbital angular momentum and beyond in free-space optical communications,"  
30       *Nanophotonics* **11**(4), 645-680 (2022).
- 31  39. A. E. Willner et al., "Optical communications using orbital angular momentum beams," *Adv. Opt. Photonics*  
32       **7**(1), 66-106 (2015).
- 33  40. N. Zhao et al., "Capacity limits of spatially multiplexed free-space communication," *Nat. Photonics* **9**(12),  
34       822-826 (2015).
- 35  41. J. Mendoza-Hernández et al. Laguerre-Gauss beams versus Bessel beams showdown: peer  
36       comparison. *Opt. Lett.* **40**, 3739-3742 (2015).
- 37  42. Silverman, R. A. *Special functions and their applications*. (Courier Corporation, 1972).
- 38  43. Schmidt, J. D. *Numerical simulation of optical wave propagation: With examples in matlab* (SPIE, 2010)